Impact of Assimilating Surface Velocity Observations on the Model Sea Surface Height Using the NCOM-4DVAR*

MATTHEW J. CARRIER, HANS E. NGODOCK, PHILIP MUSCARELLA, AND SCOTT SMITH

Naval Research Laboratory, Stennis Space Center, Mississippi

(Manuscript received 8 September 2014, in final form 8 December 2015)

ABSTRACT

The assimilation of surface velocity observations and their impact on the model sea surface height (SSH) is examined using an operational regional ocean model and its four-dimensional variational data assimilation (4DVAR) analysis component. In this work, drifter-derived surface velocity observations are assimilated into the Navy's Coastal Ocean Model (NCOM) 4DVAR in weak-constraint mode for a Gulf of Mexico (GoM) experiment during August–September 2012. During this period the model is trained by assimilating surface velocity observations (in a series of 96-h assimilation windows), which is followed by a 30-day forecast through the month of October 2012. A free-run model and a model that assimilates along-track SSH observations are also run as baseline experiments to which the other experiments are compared. It is shown here that the assimilation of surface velocity measurements has a substantial impact on improving the model representation of the forecast SSH on par with the experiment that assimilates along-track SSH observations directly. Finally, an assimilation experiment is done where both along-track SSH and velocity observations are utilized in an attempt to determine if the observation types are redundant or complementary. It is found that the combination of observations provides the best SSH forecast, in terms of the fit to observations, when compared to the previous experiments.

1. Introduction

Accurate representation of the sea surface height is an important aspect of any operational ocean forecasting system. In the deep ocean, and in the absence of strong surface wind forcing, the ocean is in quasigeostrophic balance where the gradient of the SSH defines the surface currents. Events such as surface oil spills, tracking of downed aircraft, or searching for lost ships or persons at sea are directly affected by surface ocean currents. Accurate prediction of SSH can be difficult, however, as ocean mesoscale eddies (which account for much of the ocean SSH variability) are nondeterministic and small errors in the model grow over time rendering lengthy prediction impossible without regular correction by the assimilation of observations (Jacobs et al. 2014). Ocean circulation models, such as the Navy Coastal Ocean Model (NCOM; Martin 2000; Barron et al. 2006), the Hybrid Coordinate Ocean Model (HYCOM; Bleck 2002), Princeton Ocean Model (POM; Blumberg and Mellor 1987), and the Regional Ocean Modeling System (ROMS; Shchepetkin and McWilliams 2003, 2005; Marchesiello et al. 2001), among others, use widely available sea surface height anomaly (SSHA) measurements from satellite altimeters to regularly correct the model SSH.

There exist a number of methods for assimilating satellite altimeter data into ocean models. One general method involves adjusting the subsurface thermodynamic structure of the model (i.e., Haines 1991; Cooper and Haines 1996; Fox et al. 2002) in order to generate adjustments to the SSH. These methods are mainly employed with less sophisticated data assimilation (DA) methods, such as optimal interpolation (OI) or three-dimensional variational data assimilation (3DVAR), when a multivariate background error covariance is not easily attainable. More advanced methods that are capable of providing a multivariate background error covariance, either directly or through the action of an adjoint (AD) and tangent linear (TL) model, are

* Naval Research Laboratory Contribution Number NRL/JA/7320-14-2292.

Corresponding author address: Matthew J. Carrier, Naval Research Laboratory, Bldg. 1009 Balch Blvd., Stennis Space Center, MS 39529.
E-mail: matthew.carrier@nrlssc.navy.mil

DOI: 10.1175/MWR-D-14-00285.1

capable of assimilating altimeter data without resorting to empirical derivation of subsurface structures. In these cases, the altimeter data are either assimilated as an interpolated map product, such as in Moore et al. (2011), Zavala-Garay et al. (2012), or Xu et al. (2013), among others, or as a direct assimilation of along-track observations, as in Hoteit et al. (2013). Regardless of whether one uses along-track or interpolated data, it remains that one must convert the anomaly measurement to the form of the ocean model in order to assimilate the data. Doing so requires knowledge of the geoid, which can only be estimated, to convert the anomaly information into dynamic height. In practice, a long-term mean from observations or a numerical model is used as a proxy for the geoid (Chassignet et al. 2007).

Ocean velocity observations have the potential to provide information regarding the shape and gradient of the ocean SSH, without the need to derive an estimate of the geoid. Observing systems, such as Acoustic Doppler Current Profilers (ADCP), high-frequency (HF) radar, and surface ocean drifters, such as NOAA drifting buoys, can provide information on ocean currents. Let us consider the case of surface drifters. It is well known that surface currents are generally in quasigeostrophic balance with the dynamic ocean height field, except in cases of strong surface wind forcing, or near the coastlines where river inflow and offshore winds play a role. Therefore, in the absence of strong surface winds and for locations far from shore, a passive surface drifter will follow the contours of the SSH and the speed of the drifter provides information regarding the gradient of this field. The question becomes, then, can surface velocity observations help to constrain the model SSH field in the absence of along-track SSH observations? Further, can along-track SSH observations be combined with in situ surface velocity data to further improve the model forecast of SSH?

A recent experiment, dubbed the Grand Lagrangian Deployment (GLAD), was conducted in the Gulf of Mexico (GoM) in the latter half of 2012 by the Consortium for Advanced Research on Transport of Hydrocarbon in the Environment (CARTHE). Roughly 300 Coastal Ocean Dynamics Experiment (CODE)-type surface drifters (drogued to 1 m) were released in July 2012, and their positions were tracked through the GoM for the remainder of the year (Poje et al. 2014). These drifters reported their positions every 5 minutes, making the estimation of accurate Eulerian velocities possible. An earlier effort by Carrier et al. (2014) utilized the Navy's Coastal Ocean Model (NCOM) 4DVAR analysis system to assimilate Eulerian velocity estimates derived from the GLAD drifters with NCOM forecasts of the GoM. The results showed substantial improvement in the model forecast of surface currents in the vicinity of the GLAD drifters, with skill out to 96 h. In doing so, Carrier et al. (2014) demonstrated the feasibility of surface drifter–derived velocity assimilation and prediction. In this current work, we perform additional experiments and expand the analysis begun in Carrier et al. (2014) to quantitatively assess the impact of velocity assimilation on the model SSH. To that end, four experiments are presented in this work: 1) an assimilation of GLAD-derived surface velocity observations, 2) an assimilation of along-track SSH observations, 3) a combined assimilation of GLAD-derived velocities and along-track SSH, and 4) a nonassimilative free run. The results from these experiments are examined and compared to observations.

In the next section the model, assimilation system, and the observations are introduced; section 3 presents an overview of the GoM circulation during the experiment time frame; and the experiment design, results, and conclusions are given in section 4, followed by a summary in section 5.

2. Dynamical model, analysis system, and observations

a. *Dynamical ocean model*

The dynamical model used for this work is NCOM, which is a primitive equation ocean model with a free surface and a generalized vertical coordinate that can be configured with terrain-following free sigma or fixed sigma, or constant z-level surfaces in a number of combinations (Barron et al. 2006). The model employs the Mellor–Yamada level-2.5 turbulence closure parameterization (Mellor and Yamada 1982) for vertical diffusion and the Smagorinsky scheme (Smagorinsky 1963) for horizontal diffusion.

The model domain for all experiments extends from 79°–98°W to 18°–31°N using a spherical coordinate projection at a horizontal resolution of 6 km. The model has 50 layers in the vertical extending down to a maximum of 5500 m. Lateral boundary conditions for each experiment are provided by the global NCOM at 1/8° resolution; global NCOM does not include the effect of tides. For this study the 24-h forecast from global NCOM, valid on 1 August 2012, is used to provide the initial condition; this is done for the very reason that it is not as good as the analysis field, but is very close to it, so that the improvements gained from the data assimilation will be more apparent. It should be noted that the global NCOM model has the same vertical structure as the regional model used in this study (only the resolution in the horizontal is different). The global NCOM was, as of August 2012, the operational global forecasting model

used by the U.S. Navy (Barron et al. 2006). It was an assimilative model, using the multivariate optimal interpolation (MVOI) Navy Coupled Ocean Data Assimilation (NCODA) system (Cummings 2005). Analysis updates were generated every 24 h using observations in a ±12-h window around the analysis time. Surface atmospheric forcing, such as wind stress, atmospheric pressure, and surface heat flux is provided by the 0.5° NOGAPS model every 3 h (Rosmond et al. 2002); river forcing is provided via an internal NRL river product that includes monthly mean river data for each major river across the globe. There is no tidal forcing added to the boundary conditions for these experiments.

b. Ocean analysis system

The DA system selected for this work is the NCOM-4DVAR developed using the dynamical core of NCOM. The NCOM-4DVAR is a variational assimilation system based on the indirect representer method as described by Bennett (1992, 2002) and Chua and Bennett (2001). This system has been described in detail by Ngodock and Carrier (2013) and Ngodock and Carrier (2014), therefore, only a brief description is provided here. The representer method aims to find an optimal analysis solution as the linear combination of a first guess (i.e., prior model solution) and a finite number of representer functions, one per datum:

$$\hat{u}(x,t) = u_F(x,t) + \sum_{m=1}^{M} \hat{\beta}_m r_m(x,t), \tag{1}$$

where $\hat{u}(x, t)$ is the optimal analysis solution, $u_F(x, t)$ is the prior forecast, $r_m(x, t)$ is the representer function for the mth observation, and $\hat{\beta}_m$ is the mth representer coefficient. The representer coefficients can be found by solving the linear system:

$$(\mathbf{R} + \mathbf{O})\beta = \mathbf{y} - \mathbf{H}\mathbf{x}^f, \tag{2}$$

where $\mathbf{O}$ is the observation error covariance, $\mathbf{y}$ is the observation vector, $\mathbf{H}$ is the linear observation operator that maps the model fields to the observation locations, $\mathbf{x}^f$ is the model vector, and $\mathbf{R}$ is the representer matrix and is equivalent to $\mathbf{HMBM}^{\mathrm{T}}\mathbf{H}^{\mathrm{T}}$ ($\mathbf{M}$ is the TL model; $\mathbf{M}^{\mathrm{T}}$ is the adjoint model; $\mathbf{B}$ is the initial condition or model error covariance, depending on what portion of the $\mathbf{y} - \mathbf{H}\mathbf{x}^f$ vector it is applied to; and the superscript T denotes the linear transposition). Since the matrix $\mathbf{R} + \mathbf{O}$ is symmetric and positive definite, (2) can be solved for β iteratively using a linear solver, such as the conjugate gradient method. From (2) it is clear that the $\hat{\beta}_m$ for each representer can be found by integrating the adjoint and TL models over some number of minimization steps until convergence. Once found, $\hat{\beta}_m$ is acted upon in (1), involving one final sweep through the adjoint and TL models to find the analysis increment.

The background and model error covariance in NCOM-4DVAR follow the work of Weaver and Courtier (2001) and Carrier and Ngodock (2010), where the error correlation portion of the covariance, for both the model and the background errors, are not directly calculated and stored in NCOM-4DVAR; rather, the *effect* of the correlation matrix acting on an input vector is modeled by the solution of a diffusion equation. For a full explanation of this method, we refer the reader to Weaver and Courtier (2001) or Yaremchuk et al. (2013); for a description of the implementation of this method in NCOM-4DVAR, we refer the reader to Carrier and Ngodock (2010) or Ngodock (2005).

The multivariate and anisotropic characteristics of the 4DVAR error covariance are achieved by the linear dynamical balance relationships that are part of the AD and TL models. Methods based on 3DVAR attempt to model the multivariate error covariance by way of empirical balance operators (Weaver et al. 2005), whereas ensemble methods rely on the ensemble covariance itself to provide these connections (Ngodock et al. 2006). In the case of how velocity observations can impact the model SSH, the NCOM-4DVAR has two primary mechanisms: geostrophic balance and continuity.

For the geostrophic balance we can examine the NCOM momentum equations, which are expressed as

$$\frac{\partial u}{\partial t} = -\nabla\cdot(\mathbf{v}u) + Qu + fv - \frac{1}{\rho_o}\frac{\partial p}{\partial x} + F_u + \frac{\partial}{\partial z}\left(K_M\frac{\partial u}{\partial z}\right)$$

and

$$\frac{\partial v}{\partial t} = -\nabla\cdot(\mathbf{v}v) + Qv - fu - \frac{1}{\rho_o}\frac{\partial p}{\partial y} + F_v + \frac{\partial}{\partial z}\left(K_M\frac{\partial v}{\partial z}\right), \tag{3}$$

where u and v are the velocity components, Q is the volume flux source term, f is the Coriolis parameter, p is the pressure, ρ_o is the reference water density, F is the horizontal mixing term for momentum, and K_m is the vertical eddy coefficient for momentum. Let us consider just the horizontal pressure gradient component of (3) and take its first-order derivative:

$$\frac{\partial \delta u}{\partial t} = \cdots - \frac{1}{\rho_o}\frac{\partial \delta p}{\partial x} + \cdots \quad \text{and}$$
$$\frac{\partial \delta v}{\partial t} = \cdots - \frac{1}{\rho_o}\frac{\partial \delta p}{\partial y} + \cdots, \tag{4}$$

with its adjoint as

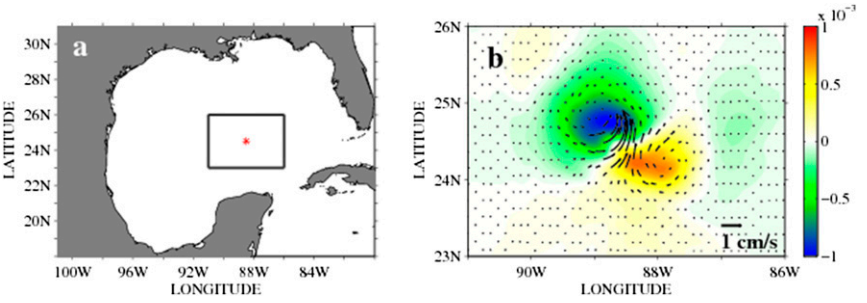

FIG. 1. (a) NCOM Gulf of Mexico domain with location of Dirac Delta impulse indicated by red star and (b) SSH cross correlation (color) with velocity perturbations (arrows) overlaid at end of 96-h TL model integration.

$$-\frac{\partial \lambda_p}{\partial t} = \frac{1}{\rho_o}\left(\frac{\partial \lambda_u}{\partial x} + \frac{\partial \lambda_v}{\partial y}\right). \tag{5}$$

It is clear from (5) that a forcing on the adjoint velocity field (λ_u and λ_v) will result in an update for the adjoint pressure variable λ_p. The horizontal gradient of the pressure field is defined in NCOM as

$$\frac{1}{\rho_o}\frac{\partial p}{\partial x} = \frac{1}{\rho_o}\frac{\partial p(\zeta)}{\partial x} + g\frac{\partial \zeta}{\partial x} + \frac{g}{\rho_o}\int_z^\zeta \frac{\partial \rho}{\partial x} dz \quad \text{and}$$
$$\frac{1}{\rho_o}\frac{\partial p}{\partial y} = \frac{1}{\rho_o}\frac{\partial p(\zeta)}{\partial y} + g\frac{\partial \zeta}{\partial y} + \frac{g}{\rho_o}\int_z^\zeta \frac{\partial \rho}{\partial y} dz, \tag{6}$$

where ζ is the surface elevation and g is gravity. Examining the components involved with the horizontal pressure gradient due to differences in the surface elevation and taking its first-order derivative gives

$$\frac{1}{\rho_o}\frac{\partial \delta p}{\partial x} = \cdots + g\frac{\partial \delta \zeta}{\partial x} + \cdots \quad \text{and}$$
$$\frac{1}{\rho_o}\frac{\partial \delta p}{\partial y} = \cdots + g\frac{\partial \delta \zeta}{\partial y} + \cdots, \tag{7}$$

and its adjoint is given as

$$-\frac{\partial \lambda_\zeta}{\partial x} = -\rho_o g\frac{\partial \lambda_p}{\partial x} \quad \text{and}$$
$$-\frac{\partial \lambda_\zeta}{\partial y} = -\rho_o g\frac{\partial \lambda_p}{\partial y}. \tag{8}$$

Therefore, from (5) and (8), a forcing on adjoint velocity will propagate to the adjoint of the pressure gradient, which in turn will force the adjoint of the surface elevation (i.e., SSH) via the adjoint of the geostrophic balance relationship. In practice, the adjoint solution is used to initialize the TL model, and therefore the TL SSH field receives this perturbation and propagates it forward in time.

The TL model provides its own mechanism for velocity observation information to influence the SSH field during the forward integration of the NCOM-4DVAR. In NCOM the depth-integrated momentum and continuity equations are needed to calculate the surface elevation. The depth-integrated continuity equation is given as

$$\frac{\partial \zeta}{\partial t} = -\frac{\partial (D\overline{u})}{\partial x} - \frac{\partial (D\overline{v})}{\partial y} + D\overline{Q}, \tag{9}$$

where D is the total depth, $\overline{Q}$ is the depth-integrated volume flux source term, and $\overline{u}$ and $\overline{v}$ are depth-integrated baroclinic velocity terms. The linearization of (9) is straightforward and indicates that the TL velocity components will induce a perturbation on the TL surface elevation. It is through these dynamical balance relationships, based on the nonlinear NCOM, that the NCOM TL and AD models are able to extract accurate sea surface height adjustments from surface velocity observations.

One can examine this feature in isolation by performing one run of the AD and TL models using a pair of impulses on one set of the adjoint velocity components. These impulses are defined as Dirac delta functions centered at the observation locations, or a single point in the model domain. The AD model is then integrated backward to the initial time, the result is convolved by the appropriate covariance functions and is used to force the TL model forward to the end of the integration time. Figure 1a shows a map of the NCOM GoM domain. The red star indicates the location of a Dirac impulse forcing to the adjoint model; in this case, Dirac impulses are placed on the u- and v-velocity components. Figure 1b shows the resulting cross correlation of velocity to SSH (with velocity perturbations overlaid) at the end of the integration window, which in this case is 96 h. The cross correlation to SSH shown here is strictly due to the propagation of the velocity information through the linearized model dynamics; there is no external forcing (surface, boundary) added to the TL and AD models. Since the Dirac impulses placed on

the velocity components were both positive unit values, the resulting velocity field is oriented toward the northeast with a perturbation on SSH that forms a dipole structure, with a positive (negative) height anomaly to the southeast (northwest) of the initial impulse location. The asymmetric appearance of the structure is due to the influence of the background state (around which the TL model is linearized). A similar pattern can be generated by employing a Dirac impulse on the SSH variable (not shown).

c. *GLAD and SSH observations*

The observations used in this study are the GLAD-derived surface velocity observations as well as altimeter derived estimates of the sea surface height. The derivation of surface velocities from the GLAD data involves the calculation of the position difference of the drifter over some time scale. In practice, however, the calculation is more complicated due to noisy position values and nonphysical accelerations. Because of this, a multistep process is used to derive Eulerian velocities from the GLAD drifter position data. The details of the processing can be found in Carrier et al. (2014) and Muscarella et al. (2015). The result of this processing is a dataset of surface velocity observations available in 15-min intervals for each drifter. The observations are given an error standard deviation value of $0.02\,\mathrm{m\,s^{-1}}$ (Carrier et al. 2014).

Altimeter data are obtained from an array of polar-orbiting satellites. These data are processed through the Altimeter Processing System (ALPS; Jacobs et al. 2002), which is available from the Altimetry Data Fusion Center (ADFC) at the Naval Oceanographic Office (NAVOCEANO). These data are stored as SSHA values and must be converted to SSH in order to be assimilated by NCOM-4DVAR. In this case a 3-yr mean SSH from a global HYCOM model run from 2008 to 2011 is used to estimate the geoid. An observational error of 5 cm for SSHA is used in this study; it does not take into account the error in the geoid estimate.

3. Gulf of Mexico circulation August–September 2012

As mentioned earlier, the GoM is the region in which the CARTHE group deployed their 300 surface drifters in an attempt to gather observational data on the near-surface circulation of the Gulf. This is an interesting region for such work, as the GoM is a semienclosed basin that is dominated by a strong current entering through the passage between the Yucatan Peninsula and the island of Cuba (Yucatan Current) and exiting through the Straits of Florida (Florida Current); this current is known as the Loop Current (LC). The LC extension into the GoM can be minor, with the current moving from the Yucatan Channel to the northeast directly to the Florida Straits (known as ''port to port''). At times, however, the LC can extend far into the GoM, either to 26°N (average extension), or as far north as 28°N (fully extended; Leben 2005). When the LC is fully extended a warm-core anticyclonic Loop Current Eddy (LCE) can be formed by the completion of the circulation around the northernmost extent of the LC. This eddy can detach and reattach many times before the LCE separates for good. Once the LCE separates, the LC returns to its port-to-port position while the LCE propagates westward at about 2–$5\,\mathrm{km\,day^{-1}}$. One possible mechanism for the detachment of the LCE from the LC is the propagation of a cold-core cyclonic eddy southwestward from the west Florida shelf, known as a Loop Current Frontal Eddy (LCFE; Schmitz 2005). This cyclonic eddy moves into the eastern side of the LC and can penetrate deep to the west, eventually resulting in the detachment of the LCE from the LC.

We can examine the LC during the experiment time period presented here using the 1/3° × 1/3° mapped absolute dynamic topography (MADT) from the Archiving, Validation, and Interpretation of Satellite Oceanographic data (AVISO; produced by Ssalto/*Duacs* and distributed by AVISO, with support from CNES at http://www.aviso.oceanobs.com/duacs/). The MADT has been calibrated to ensure that the spatial mean matches that from the daily averaged free-run NCOM (initial condition from global NCOM on 1 August, with no data assimilation thereafter; the boundary conditions are listed in the previous section); the calibration is essentially an offset to the MADT. This calibrated AVISO MADT will be referred to as AVISO SSH.

Figure 2 shows the GoM SSH for 1 August, 20 August, 10 September, and 30 September for AVISO (Figs. 2a–d) and the free-run NCOM (Figs. 2e–h). The LC on 1 August seems to be in the process of shedding a LCE and returning to its port-to-port position, with the LCE positioned near 26°N, 88°W. There appears to be a cyclonic LCFE located to the southeast of the LCE near 23.5°N, 85°W. This eddy seems to be pinching off the LC from the LCE as it extends westward, and may be partially responsible for the separation seen in the AVISO SSH. As time goes on, from 1 August to 30 September, the LCE continues to remain unattached to the LC, with the cold-core LCFE decaying slowly to its southeast. The LCE itself moves slowly westward and begins to lose amplitude, going

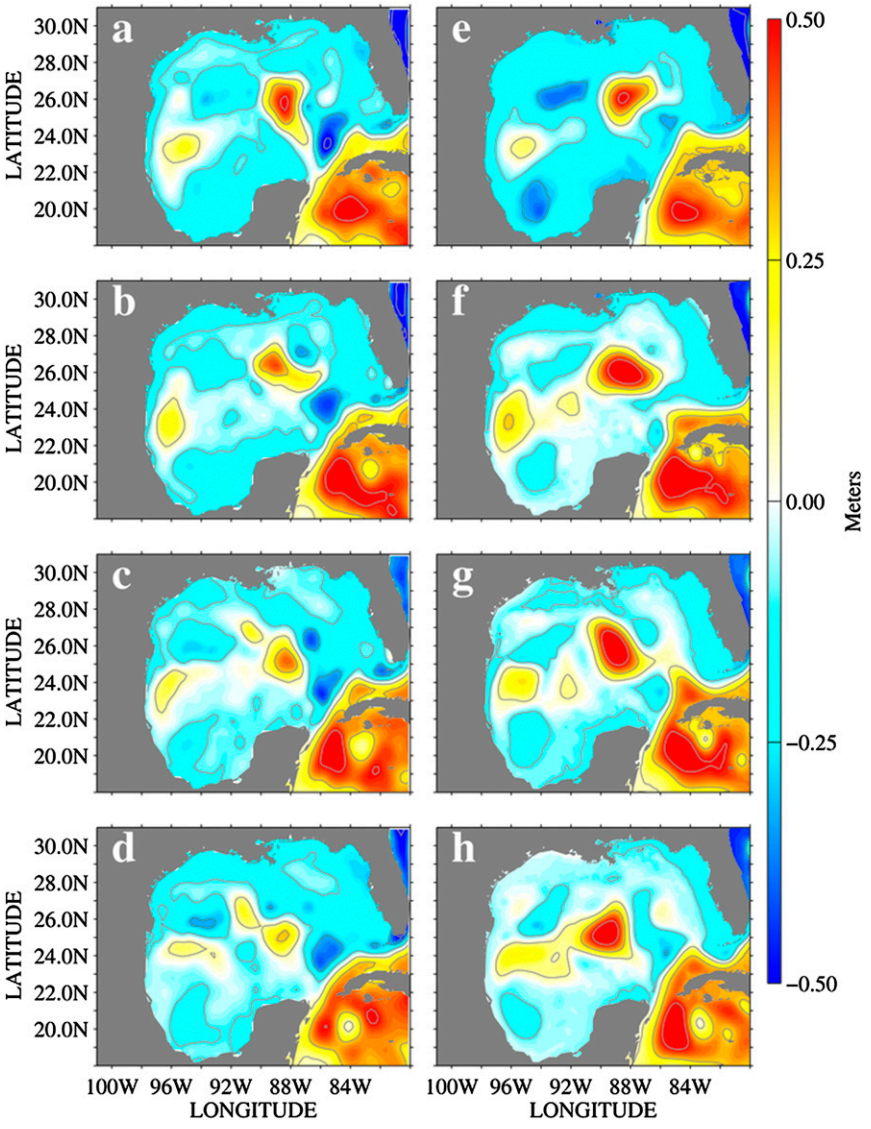

FIG. 2. Sea surface height (m) for AVISO (a) 1 Aug, (b) 20 Aug, (c) 10 Sep, and (d) 30 Sep; and for NCOM free-run (e) 1 Aug, (f) 20 Aug, (g) 10 Sep, and (h) 30 Sep.

from >0.5-m height on 1 August to below 0.25-m height by 30 September.

The NCOM free-run solution exhibits a substantially different pattern. Figure 2e shows the NCOM free-run initial condition on 1 August. The LCE, like what is seen in the AVISO SSH, seems to have detached from the LC, although its size and orientation is slightly different than the observations. The LCFE in the NCOM initial condition is much smaller than what is seen in AVISO, and in fact, has completely dissipated by 20 August (Fig. 2f). By 10 September, the LC seems to extend into the GoM again, nearly reattaching with the LCE (Fig. 2g). Finally, by 30 September (Fig. 2h), the LCE has now moved farther from the LC while maintaining a much larger size and amplitude than what is seen in AVISO. Even though the free-run experiment does not seem to be adversely affected by using the global NCOM solution as its initial condition on 1 August 2012, likely due to the marginal difference in model resolutions between the global model (roughly 12 km in the GoM) and the regional model (6 km), the global NCOM initialization is less accurate in capturing the LC and LCE positions, as well as the size, location, and amplitude of the LCFE. It is likely due to this that the free-run solution diverges quickly from reality through the remainder of the experiment. This strongly suggests that an accurate initial condition is vitally important to

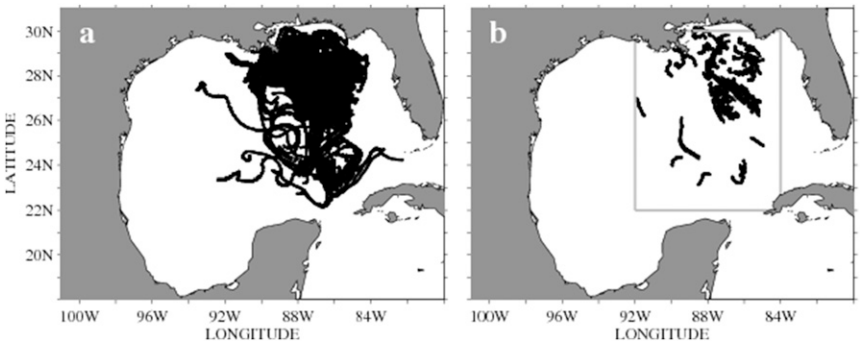

FIG. 3. (a) NCOM Gulf of Mexico domain with location of all assimilated GLAD drifter positions from 1 Aug to 30 Sep 2012 and (b) assimilated GLAD drifter positions during 2–6 Sep 2012; gray box indicates the "GLAD region" of interest.

capturing the evolution of the LC and its associated features in the GoM.

4. Experiment design and results

a. Experiment design

To assess the impact of GLAD-derived surface velocity observations on the model SSH, assimilation experiments that use surface velocity observations only (referred to here as VEL) and along-track SSH observations only (referred to here as SSH1) are run, as well as the free-run with no assimilation (referred to here as FR); a final experiment that assimilates a combination of SSH and velocity (COM) is done to determine their combined effect. Each assimilation experiment consists of a 60-day training period from 1 August to 30 September 2012; they all share the same initial condition from global NCOM on 1 August 2012. This training period proceeds as a series of 96-h assimilation windows, where at the end of each window the forecast model is run from the updated final condition to provide the background for the next 96-h assimilation cycle. Error variances and spatial correlation scales for the static covariance applied in the NCOM-4DVAR are set in the same manner as Carrier et al. (2014). As expected from any assimilation experiment attempting to correct a significantly wrong model solution (Fig. 2), it takes a few assimilation cycles before the assimilated solution begins to clearly diverge from the free run and to converge toward the observations. As a result, the subsequent analysis shown here will examine the solution for the training period from 13 August to 30 September (omitting the first three assimilation cycles during 1–12 August 2012).

Regarding the surface velocity observations, the processed GLAD velocities are available in 15-min intervals; however, these data are only assimilated hourly due to the cost of input/output (I/O) in the 4DVAR. The GLAD data are thinned at each hourly time period by the spatial correlation scale (i.e., Rossby radius, roughly 40 km in the GoM) used in the 4DVAR. This ensures that no two assimilated GLAD velocity observations are within a correlation scale of one another. Figure 3 shows the spatial distribution of the GLAD data throughout the 60-day experiment; Fig. 3a shows the total observation points through time, and Fig. 3b shows a sample distribution of assimilated observations from one 96-h assimilation window (2–6 September 2012). Figure 3 shows that the GLAD drifters are primarily contained within the central GoM for the duration of the experiment; the western GoM and the northern Caribbean Sea are mainly devoid of observations. The inhomogeneous distribution of data is likely to impact to what degree these observations modify the model SSH. Examining the SSH forecast error over the entire model domain would likely skew the results and hide this influence; therefore, our statistical analysis is done by not only examining the SSH forecast error across the entire domain, but also by concentrating on the area most densely covered by GLAD observations, hereafter referred to as the "GLAD region," indicated by the gray box in Fig. 3b. The GLAD region covers the area of the LC where mesoscale eddies are formed and shed; therefore, the circulation within the GLAD region is the most difficult to forecast.

For the SSH1 experiment, the along-track SSH observations are binned and assimilated by the NCOM-4DVAR every 6 h within each assimilation cycle. Figure 4 shows the coverage of altimeter data; Fig. 4a shows the total altimeter data assimilated over the entire experiment while Fig. 4b shows the coverage during one assimilation window (2–6 September 2012). Figure 4 shows that the GLAD region is well covered by altimeter data during the experiment, which should result in a well-constrained model SSH field within the GLAD region for the SSH1 experiment.

The 96-h forecast, generated from the 4DVAR analysis at the end of each cycle within the training period, is

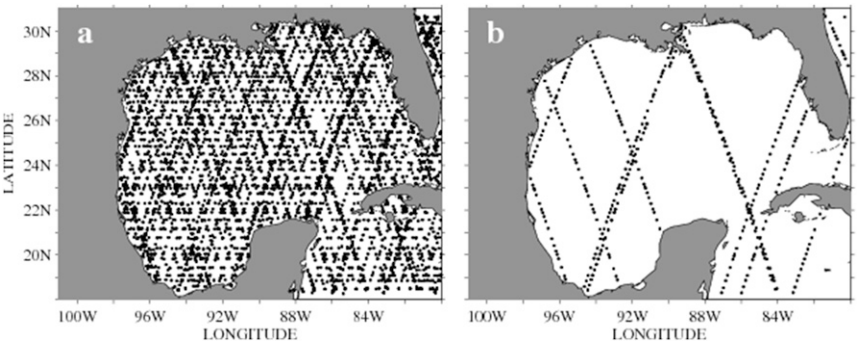

FIG. 4. As in Fig. 3, but for along-track SSH observations.

compared to available SSH observations. Along-track altimeter observations are dense in the along-track direction, but sparse in space and time in the cross-track direction; therefore, along-track altimeter observations may not capture important features at a particular instance in time. To avoid this in the forecast evaluation, the AVISO SSH has been selected as the dataset to which the forecasts will be compared. Using a composite SSH map for forecast validation is well established in the literature (Centurioni et al. 2008; Ferron 2011; Zavala-Garay et al. 2012; Xu et al. 2013; etc.) and is, therefore, appropriate for an examination of this type.

b. *Results and conclusions*

Before examining the forecast results and how they compare to observations, it is important to examine the analysis to ensure the assimilation step is functioning properly. With DA it is a reasonable requirement that the analysis fit the assimilated observations within the prescribed observation error. One can examine this by calculating a normalized mean absolute error that will be referred to here as J_{fit}. The J_{fit} metric is calculated as

$$J_{\text{fit}} = \frac{1}{M}\sum_{m=1}^{M}\frac{|y_m - H_m x^a|}{\sigma_m}, \tag{10}$$

where x^a is the model analysis, y_m is the mth observation, σ_m is the observation error, H is an operator that maps the state variables to the observation space, and M is the total number of observations. From (10) it can be shown that the analysis is fitting the observations within the prescribed observation error if the value of J_{fit} is at or less than 1.0. Figure 5 shows the J_{fit} values for the SSH for the first guess (i.e., the background 96-h forecast, FG; gray) and the analysis (AN; black) for the SSH1 experiment from 13 August to 30 September 2012 (as compared against assimilated along-track SSH observations). Each J_{fit} value is computed by comparing the first guess and analysis, valid at 0000 UTC daily, to available SSH observations that fall ±3 h around this 0000 UTC time level. Figure 5 indicates that the NCOM-4DVAR is generally fitting the along-track SSH observations within error limits for the entire experiment time frame (the value of 1.0 is indicated by the dashed line).

This check can be performed for the VEL experiment as well. Figure 6 shows the J_{fit} value for the surface velocity field for the first guess (gray) and the analysis (black) for the VEL experiment from 13 August to 30 September 2012 (cf. assimilated surface velocity observations). As with the SSH1 experiment, the VEL analysis is generally fitting the observations within the prescribed error. There is one point in late August where this is not the case, as J_{fit} values during this time are near 2.0. This coincides with the arrival of Hurricane Isaac over the northern GoM, with the storm track directly through the GLAD region. Figure 7 shows the NOGAPS surface wind stress magnitude (interpolated

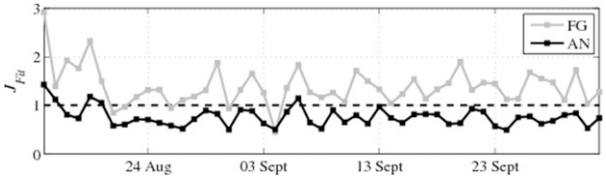

FIG. 5. The J_{fit} metric plot for SSH from the SSH1 experiment. First guess (FG) field is in gray and analysis (AN) is in black. Values computed by comparison to assimilated SSH observations from 13 Aug to 30 Sep 2012.

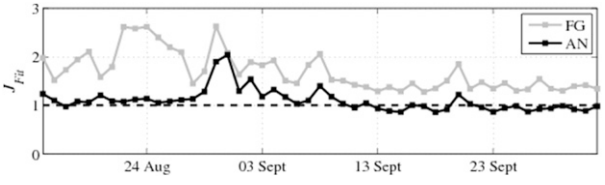

FIG. 6. The J_{fit} metric plot for velocity from the VEL experiment as compared to assimilated GLAD drifter-derived surface velocities (13 Aug–30 Sep 2012).

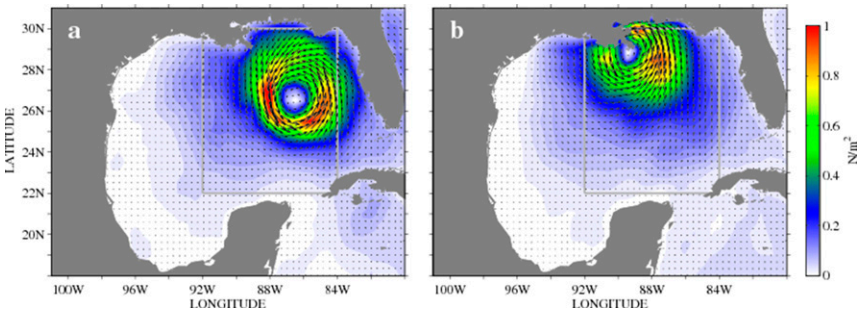

FIG. 7. NOGAPS surface wind stress (interpolated to the NCOM domain) for (a) 28 Aug and (b) 29 Aug 2012. Wind stress direction is indicated by arrows and magnitude is indicated by color contours (in $N\,m^{-2}$). GLAD region is indicated by a gray box.

to the NCOM grid) for 28 and 29 August (Figs. 7a and 7b, respectively) with wind direction indicated by curved arrows; Fig. 7 also shows the GLAD region as a gray box outline. By 28 August, the NOGAPS simulation has Isaac entering the GLAD region and making landfall later on 29 August. Hurricanes produce very strong surface wind forcing that alters surface ocean currents more toward ageostrophy. In addition to this, the surface wind forcing for NCOM is from the 0.5° NOGAPS model, a resolution that does not allow the NOGAPS model to fully capture the intensity of the surface wind. For example, on 28 August (at 0000 UTC), NOGAPS-simulated peak storm winds were $19.6\,m\,s^{-1}$, whereas the National Hurricane Center listed Isaac with winds near $31\,m\,s^{-1}$. Also, at this resolution NOGAPS is not capable of resolving small-scale features in those winds that likely have a significant impact on the surface drifters from GLAD. Thus, the background ocean state used in the assimilation does not capture the realistic ocean surface currents during this extreme weather event. Further, the prescribed model and observation errors used here in NCOM-4DVAR do not change with time. These cumulative factors are likely responsible for a poor fit to the GLAD observations in the analysis during this time period. Once the storm passed, however, the analysis fit to the surface velocity observations improves significantly and rapidly, as the J_{fit} values fall once again to and below 1.0 for the remainder of the training period. Also, the first-guess field exhibits a downward trend in error, beginning with a J_{fit} value of 3.0 on 13 August and ending with a value just above 2.0 by 30 September.

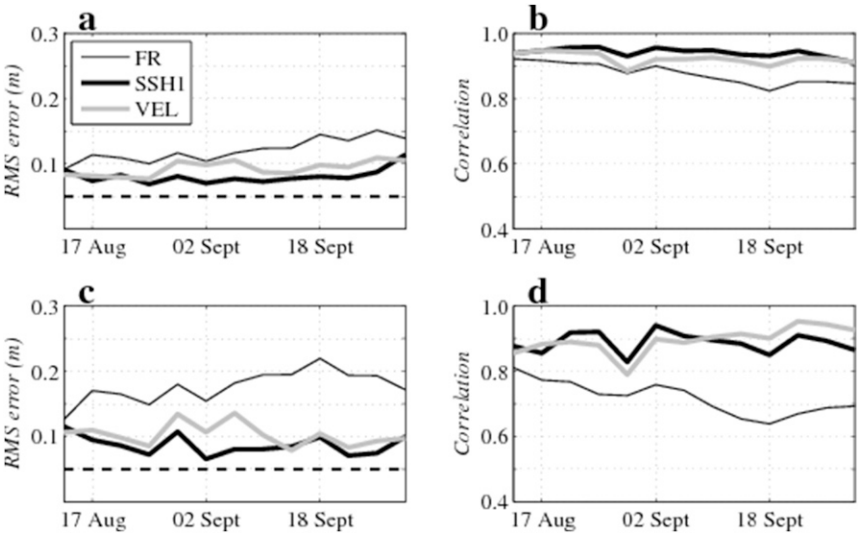

FIG. 8. RMS error over (a) entire GoM domain and (c) GLAD region only; correlation over (b) entire GoM domain and (d) GLAD region only. Statistics shown for FR (thin black), SSH1 (thick black), and VEL (gray) experiment 96-h SSH forecast solutions (cf. available AVISO SSH observations). SSH observation error indicated in (a) and (c) by dashed black line.

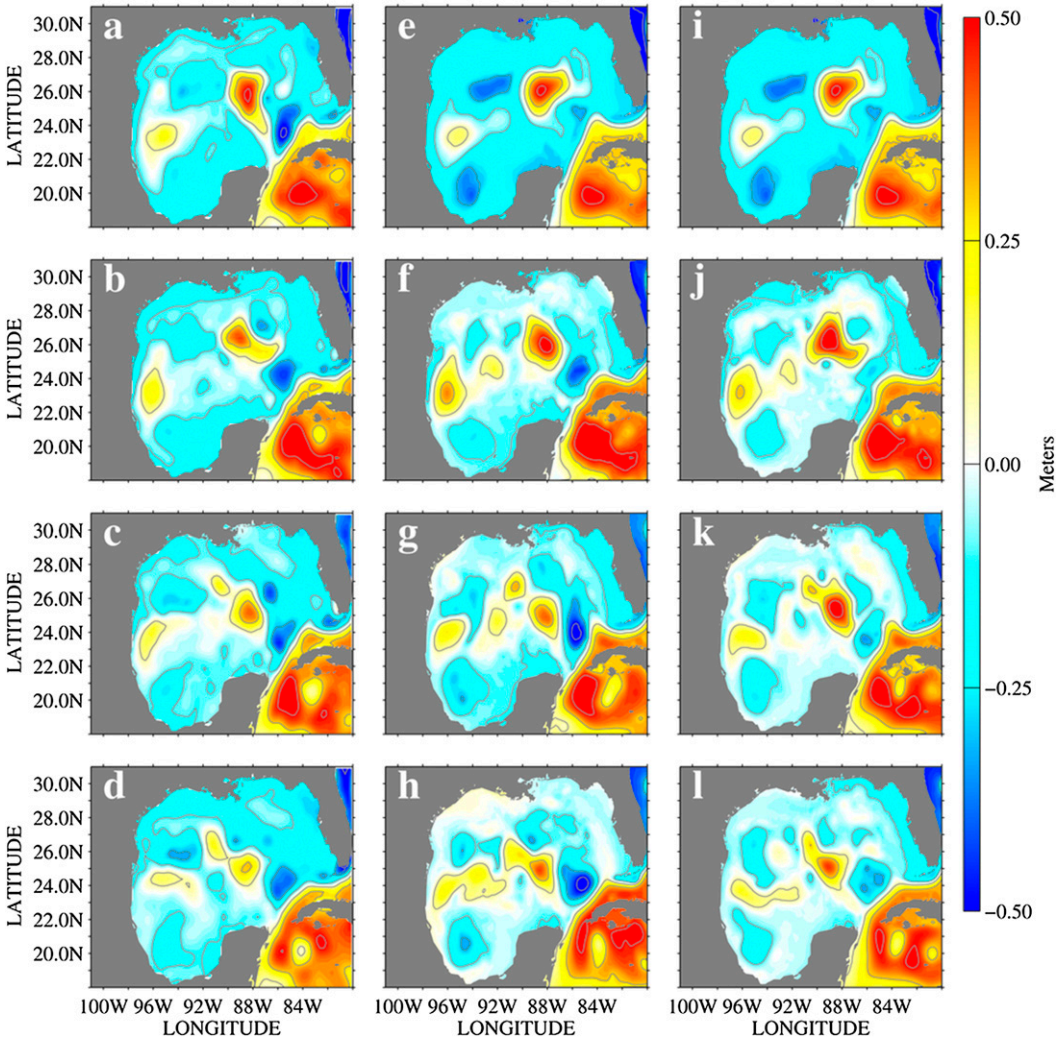

FIG. 9. Sea surface height (m) for AVISO (a) 1 Aug, (b) 20 Aug, (c) 10 Sep, and (d) 30 Sep; for SSH1 experiment (e) 1 Aug, (f) 20 Aug, (g) 10 Sep, and (h) 30 Sep; and for VEL experiment (i) 1 Aug, (j) 20 Aug, (k) 10 Sep, and (l) 30 Sep.

This indicates that the background state is improving with time as the model continues to train toward observations. The fact that this downward trend is not seen with the SSH assimilation (Fig. 5) is not surprising, as the placement of along-track SSH observations from one time to the next can be very different, whereas the GLAD observations are primarily confined to the central Gulf throughout the experiment.

An examination can be made of the model fit to AVISO during the training period from the FR, SSH1, and VEL experiments in order to ascertain if the model solution from the assimilation experiments is improved over the free run. To do this the 96-h forecast generated from each analysis during the training period is compared to the AVISO SSH. The root-mean-square (RMS) error and correlation are given as

$$\mathrm{RMS} = \sqrt{\frac{1}{M}\sum_{m=1}^{M}(y_m - H_m x^f)^2} \quad \text{and} \tag{11}$$

$$r = \frac{\sum_{m=1}^{M}(H_m x^f - X)(y_m - Y)}{\sqrt{\left[\sum_{m=1}^{M}(H_m x^f - X)^2\right]}\sqrt{\left[\sum_{m=1}^{M}(y_m - Y)^2\right]}}, \tag{12}$$

where x^f is the model forecast, X is the model mean at the observation locations (as mapped by H), and Y is the mean of the observations; and r is known as the Pearson product-moment correlation coefficient. To statistically

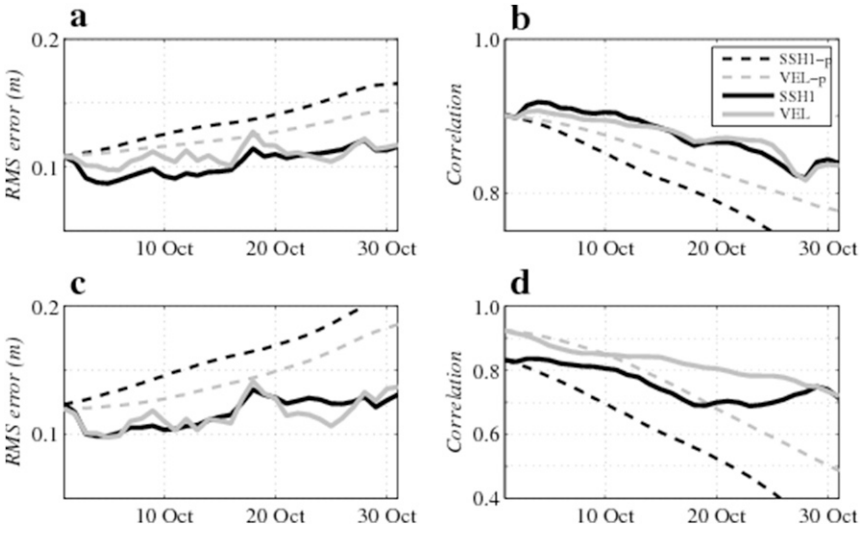

FIG. 10. (a) RMS error and (b) correlation over entire GoM domain; (c) RMS error and (d) correlation within the GLAD region. Statistics shown for SSH1 (solid black), VEL (solid gray), SSH1 persistence (dashed black), and VEL persistence (dashed gray) SSH 30-day forecast trajectory experiments (cf. available AVISO SSH observations).

compare to AVISO, the NCOM SSH fields are a daily average of the last day of each 96-h forecast. Figure 8 shows the RMS error (Figs. 8a and 8c) and correlation (Figs. 8b and 8d) for the FR (thin black), SSH1 (thick black), and VEL (gray) experiments over the whole model domain (top panels) and just within the GLAD region (bottom panels); Figs. 8a and 8c also show the prescribed SSH observation error (dashed black) for comparison. There is some improvement seen in the SSH1 and VEL experiments over the FR when examining the RMS error over the entire domain (Fig. 8a), as the FR error tops out at about 0.15 m, while the SSH1 and VEL error stay just at or slightly above 0.1 m by the end of the training period. The SSH1 seems to outperform the VEL experiment in early September, however, the error in both SSH1 and VEL when compared to AVISO becomes nearly identical by the end of the training period. Likewise, the correlation to AVISO over the entire domain is also quite comparable (Fig. 8b), with the SSH1 experiment showing slightly better correlation with AVISO than the VEL experiment. When focusing in on the GLAD region, however, there is a stark improvement in the SSH1 and VEL forecasts over the FR (Fig. 8c). The FR error reaches as high as 0.21 m, while the error in SSH1 and VEL is near 0.15 m around the time of Hurricane Isaac's passing (28–29 August) then drops to about 0.1 m by the end of the training period. Within the GLAD region, the VEL model forecast fits the AVISO SSH just as well as the SSH1 model forecast; this indicates the usefulness of the velocity observations when attempting to constrain the model SSH field. The model SSH forecast correlation to AVISO data within the GLAD region is also telling: the VEL experiment shows slightly higher correlation than the SSH1 experiment, especially through the month of September. This is likely due to the fact that the VEL experiment has many more observations, of an in situ nature, within the GLAD region than does the SSH1 experiment.

A qualitative comparison between the FR, SSH1, and VEL SSH forecasts can be made by comparing the model solutions to each other and to AVISO. Figure 9 shows a comparison of the SSH from AVISO on 1 August (Fig. 9a), 20 August (Fig. 9b), 10 September (Fig. 9c), and 30 September (Fig. 9d), to the corresponding SSH1 experiments (Figs. 9e–h) and VEL experiments (Figs. 9i–l). As was shown in Fig. 2, the initial condition obtained from global NCOM (Figs. 9e,i) shows some significant differences when compared to AVISO (Fig. 9a). It was shown how the free-run NCOM never matches AVISO throughout the experiment time frame, but with the assimilation of SSH or velocity observations, the results are quite different. Figure 9f shows the SSH1 forecast on 20 August and already the SSH field is beginning to match quite well with AVISO. The warm-core LCE eddy (26°N, 88°W) is elongated in the northwest–southeast direction, very similarly to AVISO, and the cold-core LCFE to the southeast of the LCE seen in AVISO is now apparent in the SSH1 experiment (unlike the FR). The SSH1 experiment, however, does not exhibit the ''bow'' shape in the LCE on 20 August, likely due to a weaker secondary cold-core

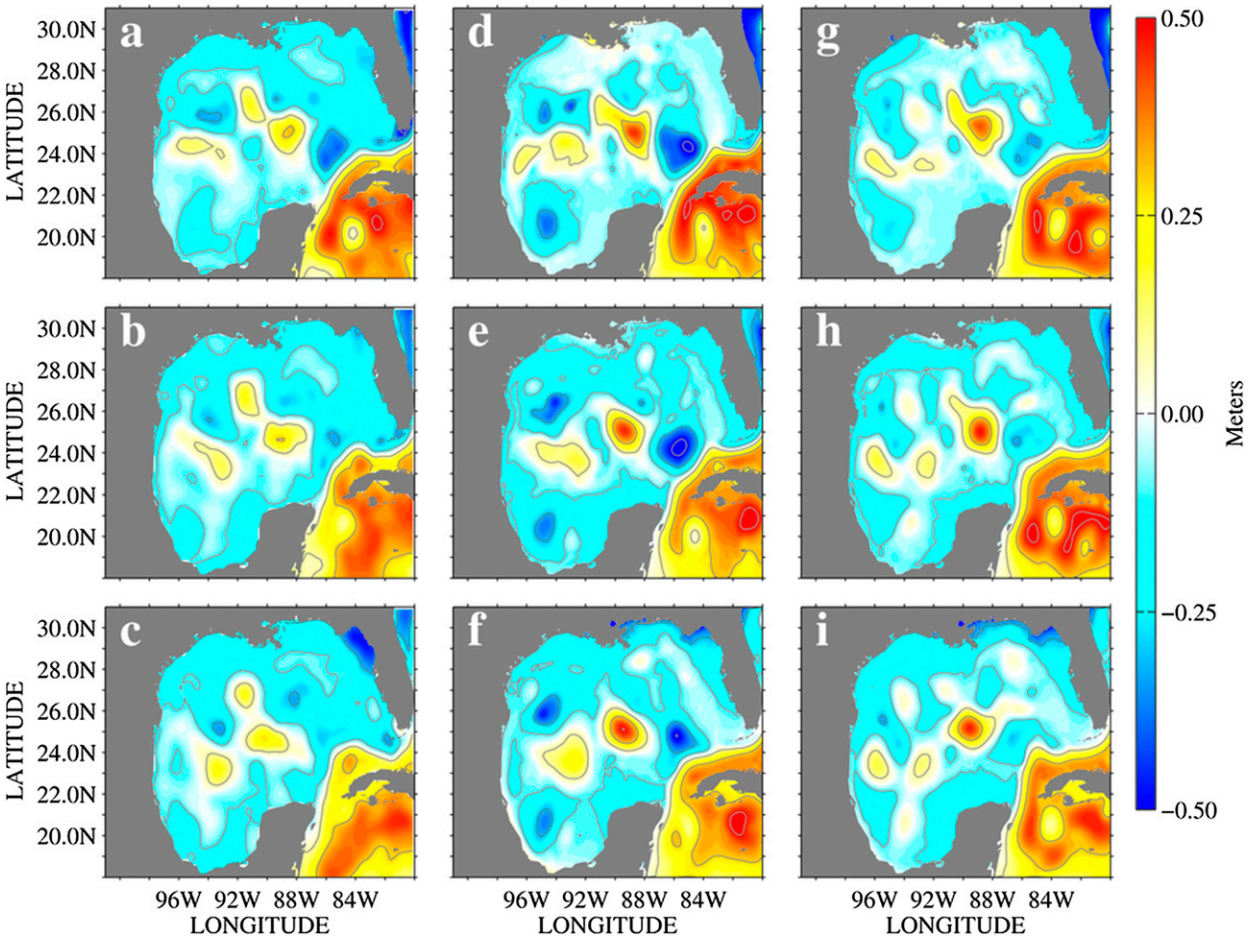

FIG. 11. Sea surface height (m) for AVISO (a) 1 Oct, (b) 15 Oct, and (c) 30 Oct; for SSH1 experiment (d) 1 Oct, (e) 15 Oct, and (f) 30 Oct; and for VEL experiment (g) 1 Oct, (h) 15 Oct, and (i) 30 Oct.

eddy to the northeast of the LCE (seen in AVISO, Fig. 9b near 27°N and 87°W). The VEL experiment, on the other hand, does seem to capture the shape of the LCE better on 20 August (Fig. 9j), albeit with greater amplitude at the eddy center. The VEL experiment does seem to capture both cold-core eddies, however, the amplitudes are lower than what is seen in AVISO. The SSH1 experiment seems to match quite well with AVISO on 10 September (Figs. 9c,g), with a dual maximum seen in the LCE and the cold-core LCFE to its southeast. However, the SSH1 experiment exhibits an LCFE (24°N, 86°W) that is deeper than what is seen in AVISO and it seems to connect this eddy with the secondary cold-core eddy (seen in Fig. 9c to the northeast of the primary LCE). Here the SSH1 experiment, unlike the FR (Fig. 2f), does not extend the LC farther into the GoM, and the LCE is not close to reattachment. This is likely due to the stronger LCFE in the SSH1 experiment than what the FR exhibits. The VEL experiment on 10 September (Fig. 9k) shows a more smoothed LCE than what is shown in AVISO or the SSH1 experiment at this time, though it is much closer to AVISO and SSH1 than the FR (Fig. 2g). The VEL experiment seems to have the dual maximum in the LCE, as in AVISO, though with a higher core amplitude. Also, the VEL experiment does exhibit the cold-core LCFE, near 24°N, 86°W, though it is weaker than what is shown in AVISO and SSH1. By the end of the training period, 30 September, the LCE in AVISO seems to be decaying, as the core amplitude has dropped significantly since 1 August (Fig. 9d). The SSH1 experiment (Fig. 9h) generally exhibits the same structure of the LCE and LCFE as seen in AVISO, but again with slightly larger amplitudes in both eddies. The VEL experiment (Fig. 9l), on the other hand, not only matches the general structure but is closer in amplitude to AVISO as well. It is important to note that the assimilation of either SSH or velocity observations seems to constrain the SSH field well (when compared to AVISO) and also helps to capture the existence of the cold-core LCFE to the southeast of the

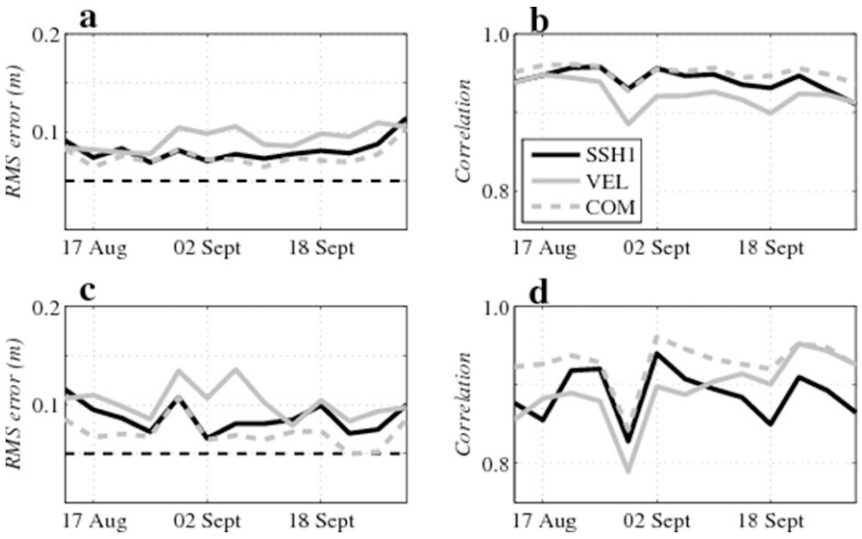

FIG. 12. RMS error over (a) entire GoM domain and (c) GLAD region only; correlation over (b) entire GoM domain and (d) GLAD region only. Statistics shown for SSH1 (thick black), VEL (gray), and COM (dashed gray) experiment 96-h SSH forecast solutions (cf. available AVISO SSH observations). SSH observation error indicated in (a) and (c) by dashed black line.

LCE, which was generally missed by the NCOM FR experiment.

It has been established that the assimilation of the GLAD-derived surface velocity observations is useful in constraining the model SSH field, nearly as well as the assimilation of along-track SSH itself. Given this, it would be useful to examine the forecast SSH error for each experiment for a longer time period than the 96 h that has been shown. Examining the forecast error out to 30 days, for instance, should shed light on the extent to which the model SSH is constrained.

For this examination, 30-day forecasts are run from the final analysis state on 30 September 2012 produced by the training period for the SSH1 and VEL experiments (using the same surface and lateral boundary forcing sources as described in section 2). The model forecast SSH is compared, as before, to the available AVISO SSH observations. Figure 10 shows the RMS error (Fig. 10a) and correlation (Fig. 10b) for the SSH1 (thick black) and VEL (gray) experiments for the entire model domain; Figs. 10c and 10d show the RMS error and correlation, respectively, for the GLAD region. The persistence forecast (i.e., nonevolving model state from 30 September) is also shown for SSH1 (dashed black; SSH1-p) and VEL (dashed gray; VEL-p) experiments. Examining the results in the full domain (Figs. 10a,b), it is clear that the forecast error for both SSH1 and VEL grows slowly through time, from 0.1 m on 30 September to just around 0.12 by 30 October (correlation dropping from 0.9 to near 0.8). The persistence forecast for SSH1 grows in error (from 0.1 to 0.15 m) more steeply than the SSH1 forecast (and correlation drops sharply, from 0.9 to below 0.8), indicating some measure of skill for the SSH1 model forecast. The same can be said for the VEL experiment, though its persistence forecast error grows less sharply. The results in the GLAD domain (Figs. 10c,d) are roughly the same, with both the SSH1 and VEL experiments exhibiting forecast skill over persistence. The FR experiment (not shown) exhibits much higher error in both the forecast and persistence than either SSH1 or VEL through all of October.

The 30-day forecasts can be examined qualitatively as well by comparing the SSH fields to each other and to AVISO. Figure 11 shows the SSH field from AVISO on 1 October (Fig. 11a), 15 October (Fig. 11b), and 30 October (Fig. 11c); also shown are the forecast SSH field from the SSH1 experiment on 1 October (Fig. 11d), 15 October (Fig. 11e), and 30 October (Fig. 11f), and from the VEL experiment on 1 October (Fig. 11g), 15 October (Fig. 11h), and 30 October (Fig. 11i). Over the month of October one can see that the primary LCE continues to decay as it moves westward in the AVISO maps (Figs. 11a–c); also, by 30 October, the AVISO observations indicate that the LC is beginning to slightly extend back into the GoM. The SSH1 forecast SSH field on 1 October (Fig. 11d) seems close to that of AVISO; the primary LCE is near 25°N, 89°W with an accompanying cold-core eddy to its southeast at 24°N, 86°W. Though, it should be noted that the SSH1 forecast LC and cold-core eddies both have higher amplitudes than what is suggested by AVISO. The VEL forecast SSH

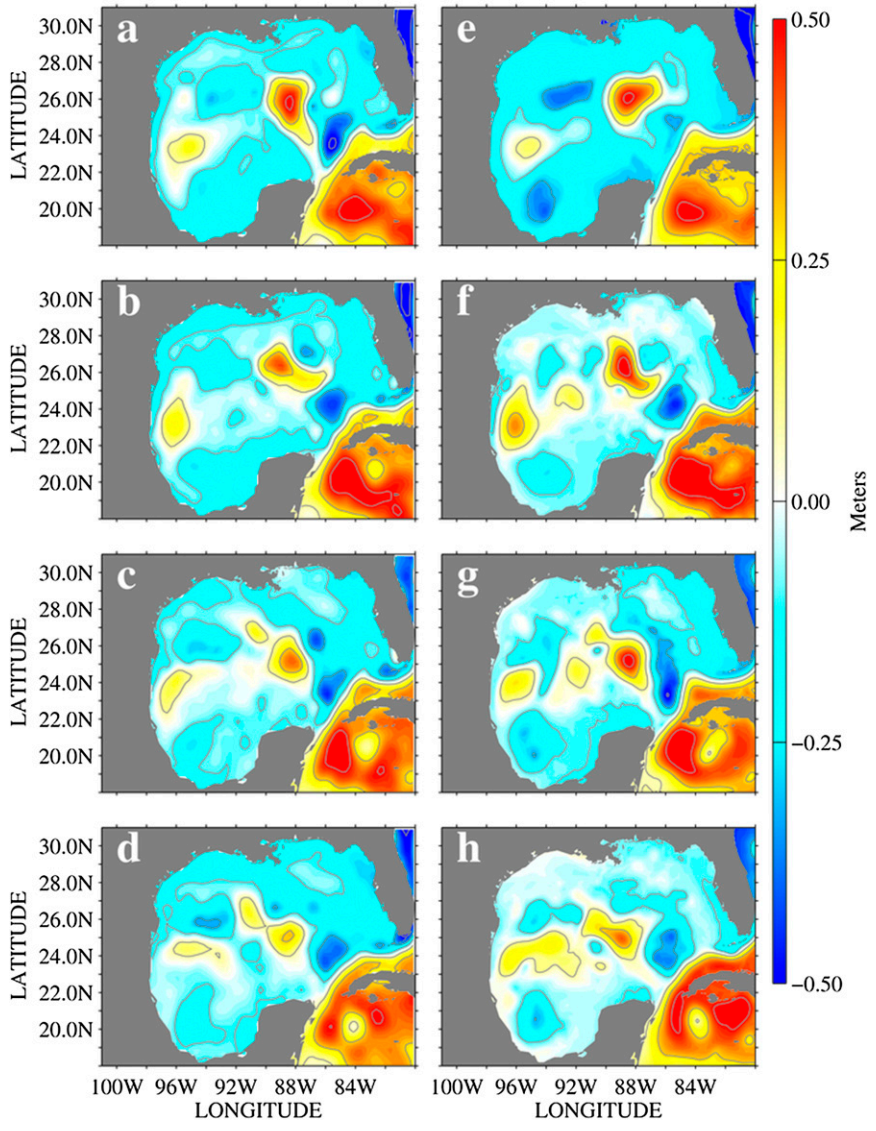

FIG. 13. Sea surface height (m) for AVISO (a) 1 Aug, (b) 20 Aug, (c) 10 Sep, and (d) 30 Sep; and for COM experiment (e) 1 Aug, (f) 20 Aug, (g) 10 Sep, and (h) 30 Sep.

field on 1 October (Fig. 11g) appears to be closer to AVISO than the SSH1 experiment. The VEL experiment LC and cold-core eddies are positioned in similar locations as those found in the SSH experiment; however, the amplitudes of these features are slightly lower in the VEL experiment when compared to the SSH experiment (especially for the cold-core eddy). This pattern continues to 15 October (Figs. 11b,e,h) as the SSH1 forecast SSH continues to exhibit higher-amplitude LC and cold-core eddies than what is seen in AVISO; meanwhile, the VEL SSH field shows a quickly decaying cold-core eddy to the southeast of the LCE, which still exhibits higher amplitude than AVISO. Finally, on 30 October (Figs. 11c,f,i), AVISO continues to show the LCE in a more decayed state than either the SSH1 or VEL model results. The SSH1 experiment continues to exhibit a relatively strong cold-core eddy to the east of the LCE, which seems to be suppressing any intrusion of the LC unlike what is seen in the AVISO observations. The VEL experiment, while still exhibiting a higher-amplitude LCE, shows that the cold-core eddy is nearly decayed and, as a possible consequence, the LC seems to be intruding somewhat northward into the southern GoM similar to AVISO. The SSH fields shown here support the statistical findings shown in Fig. 10 that suggest that the VEL forecast, while exhibiting slightly higher error than the SSH1 forecast early in October, seems to be performing as well

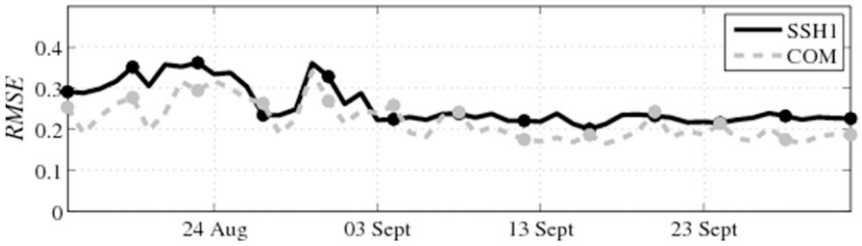

FIG. 14. NCOM surface velocity forecast RMS error for the SSH1 (thick black) and COM (dashed gray) experiments (computed using derived Eulerian velocities from GLAD drifter observations). Markers indicate the start/end of each 96-h forecast cycle.

as, if not better than, the SSH1 forecast. This suggests that the forecast error in the VEL and SSH1 experiments are roughly identical, indicating that the assimilation of velocity measurements has helped to constrain the model SSH in a comparable fashion with the SSH1 experiment.

Finally, it should be determined how the analysis and resulting forecast performs when both along-track SSH and GLAD-derived velocity observations are assimilated. This gives a sense of the added value from the inclusion of velocity observations with the standard set of temperature, salinity, and SSH observations. Figure 12 shows the RMS (Figs. 12a,c) and the correlation of each of the 96-h forecasts during the training period (Figs. 12b,d) for the SSH1 (thick black) and VEL (gray) experiments, as well as the combined assimilation (COM, dashed gray) for the entire Gulf region (top panels) and the GLAD region (bottom panels) as compared to AVISO SSH; Figs. 12a and 12c also show the prescribed SSH observation error (dashed black) for comparison. Generally, the COM SSH forecast performs closely with the SSH1 experiment throughout the Gulf (Figs. 12a and 12b), but outperforms both the SSH1 and VEL experiments within the GLAD region (Figs. 12c and 12d). This indicates that the observation types (i.e., GLAD velocities and along-track SSH) are complementary to each other. This is likely because the GLAD velocities act to ''fill in'' the gaps in the satellite coverage from the altimeters within the GLAD region. This allows for a better analysis of both the SSH and surface velocity fields and, therefore, a superior forecast as compared to assimilating either observation type alone. Figure 13 shows the qualitative comparison of the SSH field on 1 August, 20 August, 10 September, and 30 September for AVISO (Figs. 13a–d) and the COM experiment (Figs. 13e–h). The COM experiment seems to capture the primary features seen in AVISO better than the SSH1 or VEL experiments alone; for instance, on 20 August (Figs. 13b and 13f), the COM experiment not only captures the LCFE better than the VEL experiment, but it also captures the elongated ''bow'' shape to the LCE that was not captured by the SSH1 experiment. And, on 10 September (Figs. 13c and 13g), the COM experiment simulates the cold-core LCFE slightly better than the SSH1 experiment, but significantly better than the VEL experiment, while still simulating the dual maximum in the LCE. Finally, on 30 September (Figs. 13d and 13h), the COM experiment seems to capture the lower amplitude and orientation of the LCE, while also matching the LCFE in AVISO better than in the SSH1 experiment. It appears that the assimilation of GLAD-derived velocities has helped in

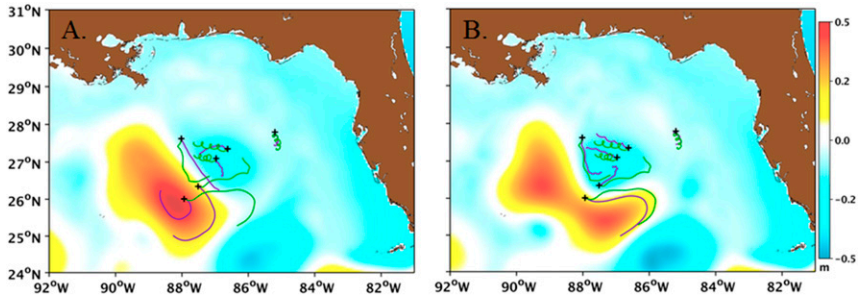

FIG. 15. The 96-h forecast SSH (color contours) and model drifter trajectories (purple) compared with observed GLAD drifter trajectories (green) for (a) SSH1 and (b) COM experiments. Forecast is valid during 21–25 Aug 2012 (SSH field shown is model average over 21–25 Aug).

the COM experiment to reduce the amplitude of the LCFE from what is seen in the SSH1 experiment. Overall, the combination of along-track SSH and velocity observations provides the best forecast compared to AVISO SSH than either the SSH1 or VEL experiments alone.

A similar examination can be made, but this time focusing on the surface velocity rather than the SSH forecast. This can be done by comparing the SSH1 and COM surface velocity forecasts against the GLAD-derived surface velocity observations. It is true that the GLAD observations are assimilated in COM, but as noted in Carrier et al. (2014), comparing the 96-h forecast trajectories to observations can be considered an independent examination as these velocities have not yet been assimilated. Figure 14 shows the RMS error for the SSH1 (thick black) and COM (dashed gray) surface velocity forecasts (line markers indicate beginning/end of each 96-h forecast trajectory). The COM experiment demonstrates superior fit to the GLAD velocity observations when compared to the SSH1 experiment, indicating that the inclusion of velocity observations in the assimilation helps to further constrain the model velocity field better than SSH observations alone. This apparent difference in the quality of the forecast velocities can be seen more clearly when examining model drifter trajectories. In this case, model drifters are initialized at the same locations as actual observed GLAD drifters. The model drifters are then advected with the model forecast velocity fields through the 96-h forecast. The trajectories over this time can be compared to the actual observed trajectories from the GLAD drifters, as was done in Muscarella et al. (2015). Muscarella et al. (2015) point out that small discrepancies in surface velocity can result in large differences in drifter trajectories. Figure 15 shows the model (purple) versus GLAD (green) drifter trajectories over one 96-h forecast time period (21–25 August, 2012) from the SSH1 (Fig. 15a) and the COM experiments (Fig. 15b); initial drifter positions are indicated by black crosses. The trajectories are overlaid on the average NCOM SSH field (color contours) from 21 to 25 August. Figure 15 clearly demonstrates that the forecast drifter trajectories from the COM experiment match the GLAD trajectories far more closely than from the SSH1 experiment. This is likely due to the effect that the additional velocity observations have on the forecast SSH structure, as the COM SSH field exhibits a slight ''L shaped'' pattern in the primary LCE (26°N, 88°W) that is not seen in the SSH1 experiment. Here, the velocity observations help to fill in the gaps between the altimeter tracks and provide a more complete estimate of the underlying mesoscale structure to the analysis, which results in the improved forecast.

5. Summary

An examination of the impact of GLAD-derived surface velocity observations on the model sea surface height in the GoM is presented. These results are compared to a free-run (i.e., no assimilation) model, to a model that assimilates the along-track SSH observations directly, and to AVISO SSH maps. The results presented here indicate that while the free-run model exhibits error growth that strongly impacts eddy positioning and amplitude by the end of the experiment time frame, the assimilation of GLAD-derived surface velocity observations can help to constrain model SSH features in a manner consistent with the assimilation of along-track SSH observations. It is further shown that a month-long forecast generated from an analysis that utilized the cycled assimilation of GLAD-derived surface velocities exhibits very similar forecast error growth when compared to a 30-day forecast generated from an analysis that used along-track SSH observations. Finally, it is demonstrated that the assimilation of both along-track SSH and velocities provides the best forecast compared to AVISO SSH, suggesting that the velocity observations are complementary to the along-track SSH and help to ''fill in'' the coverage gaps of the altimeter observations, which is especially clear when examining the model-observed drifter trajectory comparisons.

It should be noted that obtaining corrections to the sea surface height from velocity measurements is only attainable when using a sufficiently sophisticated DA system, such as the 4DVAR. Less-sophisticated assimilation methods, such as the 3DVAR, may have trouble accounting for the time-varying nature of the velocity observations, as well as the dynamical balance relationships that are required. Therefore, in order to obtain the maximum amount of useful information from velocity observations, one must account for the temporal nature of the observations as well as account for the cross covariances to each of the other model variables.

It has now been demonstrated that surface velocity observations not only help to constrain the model velocity field, but can also be used to correct the model SSH—a very important necessity, especially given the sparse nature of altimeter observations. This study suggests that targeted drifter observations can be used to help constrain the model SSH with applications in, not only large-scale forecasting, but also in regional applications (e.g., capturing the location of the loop current edge for oil rig operations).

Acknowledgments. This work was sponsored by the Office of Naval Research Program Element 0601153N as part of the "A Multiscale Approach to Assessing Predictability of ASW Environment" and "NCOM-4DVAR Rapid Transition" projects, and part of this research is funded by a grant from BP/The Gulf of Mexico Research Initiative to the Consortium for Advanced Research on the Transport of Hydrocarbon in the Environment (CARTHE). The authors would like to acknowledge Emanuel Coelho for his work in processing the GLAD drifter observations into Eulerian velocity observations used in this assimilation study. The authors would also like to thank the anonymous reviewers for their helpful comments and suggested revisions.

REFERENCES

Barron, C. N., A. Birol Kara, P. J. Martin, R. C. Rhodes, and L. Smedstad, 2006: Formulation, implementation and examination of vertical coordinate choices in the Global Navy Coastal Ocean Model (NCOM). *Ocean Modell.*, **11**, 347–375, doi:10.1016/j.ocemod.2005.01.004.

Bennett, A. F., 1992: *Inverse Methods in Physical Oceanography.* Cambridge University Press, 347 pp.

——, 2002: *Inverse Modeling of the Ocean and Atmosphere.* Cambridge University Press, 234 pp.

Bleck, R., 2002: An oceanic general circulation model framed in hybrid isopycnic-Cartesian coordinates. *Ocean Modell.*, **4**, 55–88, doi:10.1016/S1463-5003(01)00012-9.

Blumberg, A. F., and G. L. Mellor, 1987: A description of a three-dimensional coastal ocean circulation model. *Three-Dimensional Coastal Ocean Models*, N. Heaps, Ed., Amer. Geophys. Union, 1–16.

Carrier, M. J., and H. Ngodock, 2010: Background-error correlation model based on the implicit solution of a diffusion equation. *Ocean Modell.*, **35**, 45–53, doi:10.1016/j.ocemod.2010.06.003.

——, ——, S. Smith, G. Jacobs, P. Muscarella, T. Ozgokmen, B. Haus, and B. Lipphardt, 2014: Impact of assimilating ocean velocity observations inferred from Lagrangian drifter data using the NCOM-4DVAR. *Mon. Wea. Rev.*, **142**, 1509–1524, doi:10.1175/MWR-D-13-00236.1.

Centurioni, L. R., J. C. Ohlmann, and P. P. Niiler, 2008: Permanent meanders in the California Current System. *J. Phys. Oceanogr.*, **38**, 1690–1710, doi:10.1175/2008JPO3746.1.

Chassignet, E. P., H. E. Hurlburt, O. M. Smedstad, G. R. Halliwell, P. J. Hogan, A. J. Wallcraft, R. Baraille, and R. Bleck, 2007: The HYCOM (HYbrid Coordinate Ocean Model) data assimilation system. *J. Mar. Syst.*, **65**, 60–83, doi:10.1016/j.jmarsys.2005.09.016.

Chua, B. S., and A. F. Bennett, 2001: An inverse ocean modeling system. *Ocean Modell.*, **3**, 137–165, doi:10.1016/S1463-5003(01)00006-3.

Cooper, M., and K. Haines, 1996: Altimetric assimilation with water property conservation. *J. Geophys. Res.*, **101**, 1059–1077, doi:10.1029/95JC02902.

Cummings, J. A., 2005: Operational multivariate ocean data assimilation. *Quart. J. Roy. Meteor. Soc.*, **131**, 3583–3604, doi:10.1256/qj.05.105.

Ferron, B., 2011: A 4D-variational approach applied to an eddy-permitting North Atlantic configuration: Synthetic and real data assimilation of altimeter observations. *Ocean Modell.*, **39**, 370–385, doi:10.1016/j.ocemod.2011.06.001.

Fox, D. N., W. J. Teague, C. N. Barron, M. R. Carnes, and C. M. Lee, 2002: The Modular Ocean Data Assimilation System (MODAS). *J. Atmos. Oceanic Technol.*, **19**, 240–252, doi:10.1175/1520-0426(2002)019<0240:TMODAS>2.0.CO;2.

Haines, K., 1991: A direct method for assimilating sea surface height data into ocean models with adjustments to the deep circulation. *J. Phys. Oceanogr.*, **21**, 843–868, doi:10.1175/1520-0485(1991)021<0843:ADMFAS>2.0.CO;2.

Hoteit, I., T. Hoar, G. Gopalakrishnan, N. Collins, J. Anderson, B. Cornuelle, A. Kohl, and P. Heimbach, 2013: A MITgcm/DART ensemble analysis and prediction system with application to the Gulf of Mexico. *Dyn. Atmos. Oceans*, **63**, 1–23, doi:10.1016/j.dynatmoce.2013.03.002.

Jacobs, G. A., C. N. Barron, D. N. Fox, K. R. Whitmer, S. Klingenberger, D. May, and J. P. Blaha, 2002: Operational altimeter sea level products. *Oceanography*, **15**, 13–21, doi:10.5670/oceanog.2002.32.

——, J. G. Richman, J. D. Doyle, P. L. Spence, B. P. Bartels, C. N. Barron, R. W. Helber, and F. L. Bub, 2014: Simulating conditional deterministic predictability within ocean frontogenesis. *Ocean Modell.*, **78**, 1–16, doi:10.1016/j.ocemod.2014.02.004.

Leben, R., 2005: Altimeter-derived loop current metrics. *Circulation in the Gulf of Mexico: Observations and Models*, *Geophys. Monogr.*, Vol. 161, Amer. Geophys. Union, 181–201, doi: 10.1029/161GM15.

Marchesiello, P., J. C. McWilliams, and A. F. Shchepetkin, 2001: Open boundary conditions for long-term integration of regional oceanic models. *Ocean Modell.*, **3**, 1–20, doi:10.1016/S1463-5003(00)00013-5.

Martin, P. J., 2000: Description of the Navy Coastal Ocean Model version 1.0. NRL Rep. NRL/FR/7322/00/9962, 45 pp. [Available from NRL, Code 7322, Bldg. 1009, Stennis Space Center, MS 39529-5004.]

Mellor, G. L., and T. Yamada, 1982: Development of a turbulence closure model for geophysical fluid problems. *Rev. Geophys. Space Phys.*, **20**, 851–875, doi:10.1029/RG020i004p00851.

Moore, A. M., and Coauthors, 2011: The Regional Ocean Modeling System (ROMS) 4-dimensional variational data assimilation systems: Part II—Performance and application to the California Current System. *Prog. Oceanogr.*, **91**, 50–73, doi:10.1016/j.pocean.2011.05.003.

Muscarella, P., M. J. Carrier, H. Ngodock, S. Smith, B. L. Lipphardt, A. D. Kirwan Jr., and H. S. Huntley, 2015: Do assimilated drifter velocities improve Lagrangian predictability in an operational ocean model? *Mon. Wea. Rev.*, **143**, 1822–1832, doi:10.1175/MWR-D-14-00164.1.

Ngodock, H. E., 2005: Efficient implementation of covariance multiplication for data assimilation with the representer method. *Ocean Modell.*, **8**, 237–251, doi:10.1016/j.ocemod.2003.12.005.

——, and M. J. Carrier, 2013: A weak constraint 4D-Var Assimilation system for the Navy coastal ocean model using the representer method. *Data Assimilation for Atmospheric, Oceanic and Hydrologic Applications*, Vol. II, S. K. Park and L. Xu, Eds., Springer-Verlag, doi:10.1007/978-3-642-35088-7_15.

——, and ——, 2014: A 4DVAR system for the Navy Coastal Ocean Model. Part I: System description and assimilation of synthetic observations in the Monterey Bay. *Mon. Wea. Rev.*, **142**, 2085–2107, doi:10.1175/MWR-D-13-00221.1.

——, G. A. Jacobs, and M. Chen, 2006: The representer method, the ensemble Kalman filter and the ensemble Kalman smoother: A comparison study using a nonlinear reduced gravity ocean model. *Ocean Modell.*, **12**, 378–400, doi:10.1016/j.ocemod.2005.08.001.

Poje, A. C., and Coauthors, 2014: Submesoscale dispersion in the vicinity of the Deepwater Horizon spill. *Proc. Natl. Acad. Sci.*, **111**, 12 693–12 698, doi:10.1073/pnas.1402452111.

Rosmond, T. E., J. Teixeria, M. Peng, T. F. Hogan, and R. Pauley, 2002: Navy Operational Global Prediction System (NOGAPS): Forcing for ocean models. *Oceanography*, **15**, 99–106, doi:10.5670/oceanog.2002.40.

Schmitz, W., 2005: Cyclones and westward propagation in the shedding of anticyclonic rings from the loop current. *Circulation in the Gulf of Mexico: Observations and Models*, *Geophys. Monogr.*, Vol. 161, Amer. Geophys. Union, 241–261, doi:10.1029/161GM18.

Shchepetkin, A. F., and J. C. McWilliams, 2003: A method for computing horizontal pressure-gradient force in an oceanic model with nonaligned vertical grid. *J. Geophys. Res.*, **108**, 3090, doi:10.1029/2001JC001047.

——, and ——, 2005: The Regional Oceanic Modeling System (ROMS): A split-explicit, free-surface, topography-following-coordinate oceanic model. *Ocean Modell.*, **9**, 347–404, doi:10.1016/j.ocemod.2004.08.002.

Smagorinsky, J., 1963: General circulation experiments with the primitive equations. I: The basic experiment. *Mon. Wea. Rev.*, **91**, 99–164, doi:10.1175/1520-0493(1963)091<0099:GCEWTP>2.3.CO;2.

Weaver, A. T., and P. Courtier, 2001: Correlation modeling on the sphere using a generalized diffusion equation. *Quart. J. Roy. Meteor. Soc.*, **127**, 1815–1846, doi:10.1002/qj.49712757518.

——, C. Deltel, E. Machu, S. Ricci, and N. Daget, 2005: A multivariate balance operator for variational ocean data assimilation. *Quart. J. Roy. Meteor. Soc.*, **131**, 3605–3625, doi:10.1256/qj.05.119.

Xu, F.-H., L.-Y. Oey, Y. Miyazawa, and P. Hamilton, 2013: Hindcasts and forecasts of Loop Current eddies in the Gulf of Mexico using local ensemble transform Kalman filter and optimum-interpolation assimilation schemes. *Ocean Modell.*, **69**, 22–38, doi:10.1016/j.ocemod.2013.05.002.

Yaremchuk, M., M. Carrier, S. Smith, and G. Jacobs, 2013: Background error correlation modeling with diffusion operators. *Data Assimilation for Atmospheric, Oceanic and Hydrologic Applications*, Vol. II, S. K. Park and L. Xu, Eds., Springer-Verlag, doi:10.1007/978-3-642-35088-7_15.

Zavala-Garay, J., J. L. Wilkin, and H. G. Arango, 2012: Predictability of mesoscale variability in the East Australian Current given strong-constraint data assimilation. *J. Phys. Oceanogr.*, **42**, 1402–1420, doi:10.1175/JPO-D-11-0168.1.